

# **Thermodynamic modeling of the Pd-Zn system with uncertainty quantification and its implication to tailor catalysts**

Rushi Gong<sup>1</sup>, Shun-Li Shang<sup>1</sup>, Hui Sun<sup>1</sup>, Michael J. Janik<sup>2</sup>, and Zi-Kui Liu<sup>1</sup>

<sup>1</sup>Department of Materials Science and Engineering, The Pennsylvania State University, University Park, PA 16802, USA

<sup>2</sup>Department of Chemical Engineering, The Pennsylvania State University, University Park, PA 16802, USA

## Abstract

Pd-Zn intermetallic catalysts show encouraging combinations of activity and selectivity on well-defined active site ensembles. Thermodynamic description of the Pd-Zn system, delineating phase boundaries and enumerating site occupancies within intermediate alloy phases, is essential to determining the ensembles of Pd-Zn atoms as a function of composition and temperature. Combining the present extensive first-principles calculations based on density functional theory (DFT) and available experimental data, the Pd-Zn system was remodeled using the CALculation of PHase Diagrams (CALPHAD) approach. High throughput modeling tools with uncertainty quantification, i.e., ESPEI and PyCalphad, were incorporated in the phase analysis. The site occupancies across the  $\gamma$ -phase composition region were given special attention. A four-sublattice model was used for the  $\gamma$ -phase owing to its four Wyckoff positions, i.e., the outer tetrahedral (OT) site 8c, the inner tetrahedral (IT) site 8c, the octahedral (OH) 12e, and the cuboctahedral (CO) site 24g. The site fractions of Pd and Zn calculated from the present thermodynamic model show the occupancy preference of Pd in the OT and OH sublattices in agreement with experimental observations. The force constants obtained from DFT-based phonon calculations further supports the tendency of Pd occupying the OH sublattice compared with the IT and CO sublattice. The catalytic assembles changing from Pd monomers ( $\text{Pd}_1$ ) to trimers ( $\text{Pd}_3$ ) on the surface of  $\gamma$ -phase are attributed to the increase of Pd occupancy in the OH sublattice.

## Highlights

- Thermodynamic re-modeling of the Pd-Zn system with uncertainty quantification (UQ)
- A 4-sublattice model used to model  $\gamma$ -phase and its site occupancy
- Phonon calculations to understand site occupancy in  $\gamma$ -phase
- Surface construction in  $\gamma$ -phase examined to tailor its catalytic performance

**Keywords:** Pd-Zn system, catalysts, first-principles calculations, CALPHAD modeling

## 1 Introduction

Palladium (Pd) alloys are known for their excellent catalytic properties in a variety of reactions such as hydrogenation of alkynes (including acetylene) and butadiene <sup>1-3</sup>. By alloying with inert components such as zinc (Zn), catalytic ensembles on the surface of Pd can be controlled to enhance selectivity for semi/partial-hydrogenation reactions <sup>2,4</sup>. The Pd-Zn catalyst is also effective for other reactions, for example, methanol steam reforming and ester hydrogenation <sup>5,6</sup>.

In the Pd-Zn system, site occupancy of Pd and Zn in the gamma ( $\gamma$ ) phase offers distinct advantages for precisely controlling the composition of active sites <sup>7</sup>. In collaboration with experimental efforts in the Rioux group <sup>4</sup>, we have recently illustrated that subtle changes in composition within the Pd-Zn  $\gamma$ -phase can be used to control the surface active site between isolated Pd<sub>1</sub> and Pd<sub>3</sub> species isolated by surrounding Zn atoms. The  $\gamma$  phase has the  $\gamma$ -Cu<sub>5</sub>Zn<sub>8</sub> structure with space group  $I\bar{4}3m$  and 52 atoms per crystallographic cell in four Wyckoff sites, i.e., the outer tetrahedral (OT) site 8c, the inner tetrahedral (IT) site 8c, the octahedral (OH) 12e, and the cuboctahedral (CO) site 24g <sup>8</sup>. Adjusting compositions in the  $\gamma$  phase leads to different surface chemistry for given Miller indices, as variation in elemental site occupancies exposes different Pd-Zn arrangements on the surface. Before surface site structure can be considered, a thermodynamic description of the bulk intermetallic phase is needed. Thermodynamic description of the  $\gamma$ -phase in Pd-Zn is hence fundamental to evaluate phase stability, site occupancy, and in turn, surface constructions, which would be helpful to design active ensembles and improve selectivity for catalytic reactions.

Thermodynamic modeling of the Pd-Zn system was performed in 2006 by Vizdal et al.<sup>9</sup>. However, a two-sublattice model of  $(\text{Pd,Zn})_2(\text{Pd,Zn})_9$  was used to depict the  $\gamma$ -phase<sup>9</sup>, which is inconsistent with the aforementioned four Wyckoff positions and hence hinders the analysis of surface constructions as a function of composition. In addition, enthalpy of formation ( $\Delta_f H$ ) of the  $\gamma$ -phase measured by Amore et al.<sup>10</sup> was not considered in the previous modeling<sup>9</sup>. The  $\Delta_f H$  values of the endmember compounds in  $\gamma$ -phase modelled by Vizdal et al.<sup>9</sup> were thus less reliable due to the lack of experimental data or theoretical predictions.

In the present work, thermodynamic description of the Pd-Zn system was re-modelled using the CALPHAD (CALculation of PHase Diagram) approach<sup>11–13</sup> with new experimental data in the literature and first-principles calculations based on density functional theory (DFT); an improved description of thermodynamic properties is achieved. In particular, a four-sublattice model is implemented for the  $\gamma$ -phase based on its four Wyckoff sites with the Gibbs energy of formation for each endmember predicted by DFT-based phonon calculations. The elementary interactions that dictate site occupancies is analyzed using force constants from phonon calculations. The open source software ESPEI (Extensible Self-optimizing Phase Equilibria Infrastructure)<sup>14</sup> with the computational engine of PyCalphad<sup>15</sup> is used for the evaluation of model parameters and uncertainty quantification (UQ). Finally, the relationship between site occupancy and catalytic ensembles on the surface of the  $\gamma$ -phase is rationalized.

## 2 Review of thermodynamic properties in the Pd-Zn system

The Pd-Zn system contains 3 solution phases, i.e., liquid, FCC, and HCP, and 6 intermetallic compounds, i.e., BCC\_B2 ( $\beta$ ), FCC\_L10 ( $\beta_1$ ), Gamma ( $\gamma$ ), Pd<sub>2</sub>Zn, PdZn<sub>2</sub>, and Pd<sub>9</sub>Zn<sub>91</sub> based on

the works summarized by Vizdal et al. <sup>9</sup>. Details of these phases can be seen in Table 1, including phase name, crystallographic information, and the sublattice models of phases used in the present work.

Phase equilibrium properties of the Pd-Zn system published before 2006 were reviewed by Vizdal et al. <sup>9</sup> based on the previous assessments <sup>16,17</sup>. Massalski <sup>16</sup> reported the solubility of Zn in FCC Pd to be about  $x_{Zn} = 0.18-0.20$ , and the similar values were also observed by Hansen and Anderko <sup>17</sup>. The maximum solubility of Zn in FCC Pd was around  $x_{Zn} = 0.26$  at 1000°C reported by Chiang et al. <sup>18</sup> and Kou and Chang <sup>19</sup>. The solubility of Pd in HCP Zn was reported to be lower than  $x_{Zn} = 0.01$  <sup>9,16,17</sup>. Vizdal et al. <sup>9</sup> measured the temperatures of the invariant reactions, i.e., Liquid  $\rightarrow$  Pd<sub>9</sub>Zn<sub>91</sub> + HCP at 690 K and Liquid + Gamma  $\rightarrow$  Pd<sub>9</sub>Zn<sub>91</sub> at 707 K, in the Zn-rich region using differential thermal analysis (DTA).

Thermochemical measurements for the Pd-Zn system are scarce. Kou and Chang <sup>19</sup> measured the activities of Zn ( $a_{Zn}$ ) in  $\beta_1$ , showing that  $\ln a_{Zn}$  increases from -9.146 to -1.464 with  $x_{Zn}$  from 0.3762 to 0.5779. They also reported the enthalpies of formation of  $\beta_1$  as -66.5 kJ/mol-atom at 1000°C. Chiang et al. <sup>18</sup> measured the vapor pressures of Zn between 750 and 1300 K with  $x_{Zn} = 0 - 0.83$ , using the isopiestic method. From these measurements, they determined the activities of Pd and Zn in FCC,  $\beta$ , and  $\beta_1$  and partial molar Gibbs energy and enthalpy in  $\beta_1$  <sup>18</sup>. According to Chiang et al. <sup>18</sup>, at 1273 K, the activity values of  $\ln a_{Zn}$  increase from -15.24 to -1.48 with increasing  $x_{Zn}$  from 0.01 to 0.6; and the partial molar Gibbs energy and enthalpy reach the lowest values at  $x_{Zn}=0.5$ , which are  $-50.8 \pm 2.0$  kJ/mol-atom and  $-70.2 \pm 10.0$  kJ/mol-atom, respectively. Amore et al. <sup>10</sup> used calorimetry to obtain the enthalpy of formation between -33.7 and -35.1

kJ/mol-atom for the alloys with  $x_{Zn} = 0.77 - 0.8$ . Site occupancy in  $\gamma$  were reported by Edström et al. <sup>8</sup>, Gourdon et al. <sup>20</sup>, and Dasgupta et al. <sup>4</sup> using X-ray diffraction (XRD). The OT sites were fully occupied by Pd, the OH sites were occupied by Pd and Zn, the IT and CO sites were occupied by Zn.

### 3 Methodology

#### 3.1 DFT-based first-principles calculations

##### 3.1.1 Free energy at finite temperatures

The Helmholtz energy of a given structure,  $F(V, T)$ , is obtained as a function of volume ( $V$ ) and temperature ( $T$ ) in terms of the quasiharmonic approach by DFT-based first-principles calculations and expressed as <sup>21</sup>

$$F(V, T) = E(V) + F_{el}(V, T) + F_{vib}(V, T) \quad \text{Eq. 1}$$

where  $E(V)$  is the static energy at 0 K without the zero-point vibrational energy. The equilibrium results at zero external pressure ( $P = 0$  GPa) including static energy  $E_0$ , volume ( $V_0$ ), bulk modulus ( $B_0$ ) and its pressure derivate ( $B'$ ) were obtained using a four-parameter Birch-Murnaghan (BM4) equation of state (EOS) as shown below <sup>21</sup>

$$E(V) = a + bV^{-2/3} + cV^{-4/3} + dV^{-2} \quad \text{Eq. 2}$$

where  $a$ ,  $b$ ,  $c$ , and  $d$  are fitting parameters. In the present work, DFT calculations were performed with 8 volumes for EOS fitting with  $V/V_0$  in the range of  $0.91 \sim 1.12$ . The second term in **Eq. 1**,  $F_{el}(V, T)$ , represents the temperature-dependent thermal electronic contribution described by <sup>22</sup>,

$$F_{el}(V, T) = E_{el}(V, T) - T \cdot S_{el}(V, T) \quad \text{Eq. 3}$$

where  $E_{el}$  and  $S_{el}$  are the internal energy and entropy of thermal electron excitations, respectively, obtained from the electronic density of states (DOS). The third term in **Eq. 1**,  $F_{vib}(V, T)$ , represent the vibrational contribution given by <sup>22,23</sup>,

$$F_{vib}(V, T) = k_B T \sum_q \sum_j \ln \left\{ 2 \sinh \left[ \frac{\hbar \omega_j(q, V)}{2k_B T} \right] \right\} \quad \text{Eq. 4}$$

where  $\omega_j(q, V)$  represents the frequency of the  $j^{\text{th}}$  phonon mode at wave vector  $q$  and volume  $V$ , and  $\hbar$  the reduced Plank constant. The phonon DOS's for the phases of interest were calculated for at least 4 volumes, which cover the temperature range from 0 K to 1000 K.

### 3.1.2 Details of first-principles calculations

DFT-based first-principles and phonon calculations were performed to obtain Helmholtz energies of intermetallic compounds and endmembers at finite temperatures, which equal to Gibbs energies under ambient pressure. The Vienna *Ab initio* Simulation Package (VASP) <sup>24</sup> was employed for all DFT-based calculations. The projector augmented-wave method (PAW) was used to account for electron-ion interactions in order to increase computational efficiency compared with the full potential methods <sup>25,26</sup>. Electron exchange and correlation effects were described using the generalized gradient approximation (GGA) as implemented by Perdew, Burke, and Ernzerhof (PBE) <sup>27</sup>. The GGA includes the electronic density and its gradient as exchange-correlation functionals. Furthermore, the hybrid exchange-correlation functional HSE06 <sup>28,29</sup> was applied to calculate the enthalpy of formation with higher accuracy. The plane-wave basis cutoff energy was 277 eV for relaxations and 520 eV for the final static calculations. The convergence criterion of the electronic self-consistency was set as  $10^{-6}$  eV/atom for relaxations and static calculations.



Table 2 provides parameters for first-principles and phonon calculations, including reciprocal k-points meshes and supercell sizes for compounds Pd<sub>2</sub>Zn, PdZn, PdZn<sub>2</sub>, 16 endmembers of  $\gamma$ -phase (26 atoms for each endmember in the primitive cell of  $\gamma$ -phase), where endmember represents configuration where only one component in each sublattice<sup>30</sup>, and Pd<sub>8</sub>Zn<sub>44</sub> (the key endmember of  $\gamma$ -phase in its crystallographic cell). The phonon calculations were performed using the supercell method. The phonon DOS's and force constants were analyzed using the YPHON code<sup>31</sup>. Note that Table 2 includes the supercell sizes and k-points meshes for phonon calculations, while the plane-wave cutoff energy of 277 eV was used for phonon calculations.

### 3.2 Thermodynamic modeling

In the present work, nine phases, i.e., Liquid, FCC, HCP,  $\beta$ ,  $\beta_1$ ,  $\gamma$ , Pd<sub>2</sub>Zn, PdZn<sub>2</sub> and Pd<sub>9</sub>Zn<sub>91</sub>, are modeled based on available experimental data reviewed in Sec.2 and thermochemical data from DFT-based first-principles and phonon calculations showed in Sec.3.1. The Gibbs energy functions of pure Pd and Zn are taken from the Scientific Group Thermodata Europe (SGTE) pure element database<sup>32</sup>.

Gibbs energies of the solution phases  $\theta$  of Liquid (L), FCC, and HCP are formulated as,

$$G_m^\theta = \sum_{i=Pd,Zn} x_i {}^oG_i^\theta + RT \sum_{i=Pd,Zn} x_i \ln x_i + {}^{xs}G_m \quad \text{Eq. 5}$$

where  $x_i$  is the mole fraction of component  $i$ ,  ${}^oG_i^\theta$  the Gibbs energy of component  $i$ ,  $R$  the gas constant,  $T$  the temperature, and  ${}^{xs}G_m$  the excess Gibbs energy. The first term represents mechanical mixing of the endmembers, here the pure elements. The second term represents the

ideal configurational entropy of mixing. The third term represents the excess Gibbs energy, which is described by the Redlich-Kister polynomial <sup>33</sup>,

$${}^{xs}G_m = x_{Pd}x_{Zn} \sum_{k=0} {}^kL_{Pd,Zn}(x_{Pd} - x_{Zn})^k \quad \text{Eq. 6}$$

where  ${}^kL_{Pd,Zn}$  is the  $k^{\text{th}}$  interaction parameter between Pd and Zn, modeled as

$${}^kL_{Pd,Zn} = A + BT + CT \ln T \quad \text{Eq. 7}$$

where  $A$ ,  $B$ , and  $C$  are model parameters to be evaluated.

The BCC\_B2  $\beta$  phase (space group  $Pm\bar{3}m$  with two Wyckoff sites 1a and 1c) appears at high temperatures. Taking into account its broad solubility range with  $x_{Zn} = 0.37-0.56$  <sup>16</sup>, a two-sublattice model  $(Pd,Zn)_1(Pd,Zn)_1$  is adopted with its Gibbs energy formulated as,

$$G_m = \sum_{i=Pd,Zn} \sum_{j=Pd,Zn} y'_i y''_j {}^oG_{i,j} + RT \left( \sum_{i=Pd,Zn} y'_i \ln(y'_i) + \sum_{j=Pd,Zn} y''_j \ln(y''_j) \right) \quad \text{Eq. 8}$$

$$+ y'_{Pd} y'_{Zn} (y''_{Pd} L_{Pd,Zn: Pd} + y''_{Zn} L_{Pd,Zn: Zn})$$

$$+ y''_{Pd} y''_{Zn} (y'_{Pd} L_{Pd: Pd,Zn} + y'_{Zn} L_{Zn: Pd,Zn})$$

where  $y_i^{(s)}$  is the site fraction of component  $i$  on sublattice  $s$ ,  ${}^oG_{i,j}$  are the Gibbs energies of the endmembers ( $i:j$ ), and  $L$  are the interaction parameters, which can be expanded using the Redlich-Kister polynomials <sup>33</sup> in the same way as in **Eq. 6** and **Eq. 7**.

FCC\_L10  $\beta_1$  phase is stable at low temperatures (space group  $P4/mmm$  with two Wyckoff sites 1a and 1d). A two-sublattice model  $(Pd,Zn)_1(Pd,Zn)_1$  is applied for this phase with the Gibbs energy formula similarly to **Eq. 8**.

The  $\gamma$  phase has four Wyckoff sites (space group  $I\bar{4}3m$ ) with details presented in Sec.1. A four-sublattice model  $(\text{Pd,Zn})_2(\text{Pd,Zn})_3(\text{Pd,Zn})_2(\text{Pd,Zn})_6$  is adopted according to its Wyckoff sites (IT, 8c), (OH, 12e), (OT, 8c), and (CO, 24g), respectively. Gibbs energy of  $\gamma$  phase is written as,

$$G_m = \sum_{i=\text{Pd,Zn}} \sum_{j=\text{Pd,Zn}} \sum_{k=\text{Pd,Zn}} \sum_{l=\text{Pd,Zn}} y'_i y''_j y'''_k y''''_l G_{i;j:k:l} \quad \text{Eq. 9}$$

$$+ RT \left( 2 \sum_{i=\text{Pd,Zn}} y'_i \ln(y'_i) + 3 \sum_{j=\text{Pd,Zn}} y''_j \ln(y''_j) \right.$$

$$\left. + 2 \sum_{k=\text{Pd,Zn}} y'''_k \ln(y'''_k) + 6 \sum_{l=\text{Pd,Zn}} y''''_l \ln(y''''_l) \right) + {}^{xs}G_m$$

where  $y_i^{(s)}$  is the site fraction of component  $i$  on sublattice  $s$ ,  $s = ', ', ''',$  and  $''''$  representing the IT, OH, OT, and CO sublattice, respectively, and  ${}^{xs}G_m$  is the excess Gibbs energy. In the present work, we considered only the interaction parameters on the second sublattice (the OH site) due to the lower values of formation enthalpy for the endmembers  $(\text{Zn})_2(\text{Pd})_3(\text{Pd})_2(\text{Zn})_6$  and  $(\text{Zn})_2(\text{Zn})_3(\text{Pd})_2(\text{Zn})_6$  from DFT-based calculations (Sec.3.1) along with experimental observations<sup>8,20</sup> showing the OH site occupied by both Pd and Zn. Hence, the excess Gibbs energy is as follows

$${}^{xs}G_m = y''_{\text{Pd}} y''_{\text{Zn}} y'_{\text{Zn}} y'''_{\text{Pd}} y''''_{\text{Zn}} L_{\text{Zn:Pd,Zn:Pd:Zn}} \quad \text{Eq. 10}$$

In the present work,  $\text{Pd}_2\text{Zn}$ ,  $\text{PdZn}_2$ , and  $\text{Pd}_9\text{Zn}_9$  are treated as stoichiometric compounds (phases) with their Gibbs energies expressed as

$$G^{\text{Pd}_a\text{Zn}_b} = e^o G_{\text{Pd}}^{fcc} + f^o G_{\text{Zn}}^{hcp} + D + ET \quad \text{Eq. 11}$$

where  ${}^oG_{Pd}^{fcc}$  and  ${}^oG_{Zn}^{hcp}$  are Gibbs energies of FCC-Pd and HCP-Zn, respectively, and  $D$  and  $E$  are parameters to be evaluated.

Thermodynamic modeling of the Pd-Zn system was carried out by means of the open source software ESPEI <sup>14</sup>, which uses PyCalphad <sup>15</sup> for calculating energies of thermodynamic models. The model parameters are evaluated in two steps in ESPEI. The first step is parameter generation. In this step, the thermochemical data from DFT-based first-principles calculations with all internal degrees of freedom specified <sup>30,34</sup>, such as site fractions in each sublattice, are used to select the number of parameters and evaluate their values. The experimental thermochemical data can also be used in the first step if their internal degrees of freedom are specified, such as stoichiometric compounds or fully random solutions. This is because the minimization of Gibbs energy with respect to the internal variables is not performed in the first step. In the present work, the Gibbs energy functions of stoichiometric compounds and endmembers in the  $\beta$ ,  $\beta_1$  and  $\gamma$  phases were evaluated from DFT-based first-principles calculations with the results discussed below. In the second step, all model parameters are simultaneously optimized through the Bayesian approach using a Markov Chain Monte Carlo (MCMC) method <sup>14</sup>. The input data for the second step are primarily the experimental phase equilibrium information including two or more co-existing phases and equilibrium thermochemical data <sup>11-13</sup>. The experimental data, including phase boundary data <sup>9,16,17</sup> and thermochemical data <sup>10,18</sup>, were used to refine model parameters. In the present work, each model parameter employed two chains with a standard derivation of 0.1 when initializing in a Gaussian distribution. During the modeling process, the chain values can be tracked and the MCMC steps were performed until the model parameters converged.

The uncertainty quantification of model parameters and calculated thermodynamic properties and phase stability from the models is performed using PDUQ (Phase Diagram Uncertainty Quantification) <sup>35</sup>. PDUQ relies on the PyCalphad for predicting thermodynamic properties of interest and ESPEI for Bayesian samples to leverage the distribution of model parameters and estimate uncertainties based on the estimated Gaussian distribution of input data uncertainty <sup>14,35</sup>. The statistical distributions of model parameters are evaluated from the samples during MCMC optimization based on the Metropolis criteria <sup>14</sup>. The values from the last MCMC step were used to estimate the uncertainty. In the present work, 95% uncertainty interval (or Bayesian credible intervals containing 95% of the invariant samples) was applied to quantify the uncertainty.

## 4 Results and discussion

### 4.1 Properties of Pd-Zn compounds by first-principles calculations

Table 3 shows the predicted lattice parameters of Pd<sub>2</sub>Zn, PdZn<sub>2</sub>, and  $\gamma$  phase in the present work together with experimental data in the literature <sup>8,36–38</sup>. The lattice parameter *c* of Pd<sub>2</sub>Zn predicted from the present first-principles calculations is 7.83 Å, slightly higher than the experimental 7.65 Å <sup>36</sup>. The lattice parameters of PdZn<sub>2</sub> and  $\gamma$  are in good agreement with experimental results with the mean absolute error value around 0.027 Å.

Table 4 shows the equilibrium volume *V*<sub>0</sub>, bulk modulus *B*, and the derivative of bulk modulus *B*' obtained from the EOS *E-V* fitting at 0 K in comparison with previous DFT calculations and experimental data <sup>39</sup>. Figure 1 compares phonon DOS's of FCC-Pd, HCP-Zn, and stoichiometric compounds Pd<sub>2</sub>Zn and PdZn<sub>2</sub>. In the low-frequency region (e.g., < 3THz), HCP-Zn has the highest phonon DOS, followed by PdZn<sub>2</sub>, Pd<sub>2</sub>Zn, and FCC-Pd. The higher DOS in the low-frequency

region results in a lower average phonon frequency<sup>40</sup>. This can be confirmed by the lowest bulk modulus  $B$  of HCP-Zn compared with PdZn<sub>2</sub>, Pd<sub>2</sub>Zn, and FCC-Pd. The bulk modulus  $B$  of HCP-Zn fitted from the present work is 57.5 GPa, which is lower than PdZn<sub>2</sub> 118.1 GPa, Pd<sub>2</sub>Zn 146.0 GPa, and FCC-Pd 167.90 GPa.

Figure 2 and Figure 3 show the comparison of the entropy and enthalpy of FCC-Pd and HCP-Zn from the phonon calculations to the SGTE pure element database<sup>32</sup>. Both show excellent agreement. For results of Pd obtained from phonon calculations and SGTE, the difference of enthalpy is less than 6.5% and that of entropy is less than 5%. The results of Zn show the difference of enthalpy less than 2.1% and that of entropy less than 3.5%.

Table 5 shows the enthalpy of formation  $\Delta_f H$  at 0 K predicted from the present DFT-based calculations using the exchange-correlation functionals of GGA and HSE06, along with experimental data<sup>18,19</sup>. For the  $\gamma$  phase, the configuration of Pd<sub>10</sub>Zn<sub>42</sub> ( $x_{Zn} = 0.81$ ) was used for DFT-based calculations and compared with experimental data at  $x_{Zn}=0.80$ . The  $\Delta_f H$  value predicted using HSE06 is -33.7 kJ/mol-atom, agreeing reasonably well with -35.1 kJ/mol-atom from experiments using calorimetry<sup>10</sup>. For the  $\beta_1$  phase, the configuration of PdZn ( $x_{Zn} = 0.50$ ) was used. The  $\Delta_f H$  value of PdZn predicted using HSE06 is -69.2 kJ/mol-atom, which is in good agreement with measured  $-73.9 \pm 10$  kJ/mol-atom reported by Chiang et al.<sup>18</sup> and -66.6 kJ/mol-atom reported by Kou and Chang<sup>19</sup>, but is lower than the value predicted by GGA (-53.7 kJ/mol-atom). For both  $\gamma$  and  $\beta_1$  phases, the  $\Delta_f H$  values predicted by HSE06 are more accurate than those predicted by PBE-GGA. Considering the high computational cost, HSE06 was only applied for

key endmembers close or on the convex hull in the present work such as  $(\text{Zn})_2(\text{Pd})_3(\text{Pd})_2(\text{Pd})_6$  and  $(\text{Zn})_2(\text{Zn})_3(\text{Pd})_2(\text{Zn})_6$ .

## 4.2 Thermodynamic modeling and phase equilibria

Table 6 summarizes the model parameters of the Pd-Zn system from the present work. Figure 4 shows the calculated phase diagram in comparison with experimental data <sup>9,41,42</sup>, showing good agreement, particularly the phase boundaries of the  $\gamma$  phase. The max difference between calculated and experimental Zn compositions of the  $\gamma$  phase  $x_{\text{Zn}}^{\text{Cal}} - x_{\text{Zn}}^{\text{Expt.}}$  is around 0.016 at 892 K. The solubility range of the  $\gamma$  phase is between  $x_{\text{Zn}} = 0.775$ - $0.846$  from 300 K to 1000 K. The congruent melting temperature of the  $\gamma$  phase is 1150 K in good agreement with 1153 K suggested by Massalski <sup>16</sup>.

Table 7 lists the temperatures and compositions of invariant reactions. The experimentally reported invariant reactions, i.e., Liquid  $\rightarrow$  Pd<sub>9</sub>Zn<sub>91</sub> + HCP by Vizdal et al. <sup>9</sup> and other four invariant reactions by Massalski <sup>16</sup>, are well reproduced. The largest discrepancy is seen for the eutectic reaction, Liquid  $\rightarrow$  Pd<sub>9</sub>Zn<sub>91</sub> + HCP, i.e., 681 K calculated from the present work versus 690 K in the literature <sup>9</sup>.

Figure 5 and Figure 6 show the heat capacity, entropy, and enthalpy of stoichiometric compounds Pd<sub>2</sub>Zn and PdZn<sub>2</sub> from the present model in comparison with results from the phonon calculations. Good agreement is found, especially for enthalpy with a difference less than 4.7% for Pd<sub>2</sub>Zn and 2.8% for PdZn<sub>2</sub>. The entropy of PdZn<sub>2</sub> from phonon calculations compared with the present model shows the largest discrepancy with a difference around 6.5 J/mol-atom-K. This is because the

model parameters of stoichiometric compounds, which are obtained from first-principles calculated enthalpy and entropy, were adjusted with the experimental data of the peritectoid temperature.

Figure 7 shows the activity values of Zn at 1273 K calculated from the present model in comparison with experimental data by Chiang et al.<sup>18</sup>. The activity values of Zn in  $\beta_1$  from the present model agree well with the experiments<sup>18</sup> with the mean absolute error of  $\ln a_{Zn}$  being 0.4. A higher discrepancy occurs in the composition range  $x_{Zn} = 0.51-0.6$ . For example, at  $x_{Zn} = 0.55$ ,  $\ln a_{Zn}$  calculated from the present model is -3.52 compared with -1.56 measured by Chiang et al.<sup>18</sup>. They reported a single  $\beta_1$  phase for  $x_{Zn} = 0.52$  and a single  $\beta$  phase for  $x_{Zn} = 0.6$ . However, the present work predicts that  $\beta_1$  is in equilibrium with  $\beta$  at  $x_{Zn} = 0.52$ , and  $\beta$  is in equilibrium with liquid at  $x_{Zn}=0.6$  (see Figure 4). Figure 8 shows the activity values of Zn in FCC,  $\beta$ , and  $\beta_1$  phases, respectively, calculated from the present model with the shaded regions for uncertainty of each phase. For FCC, larger uncertainty occurs when  $x_{Zn} < 0.2$ , where the largest uncertainty is around  $\pm 15\%$  from the mean value at  $x_{Zn} = 0.02$ , and experimental data are located within this uncertainty region. For  $\beta_1$ , the experimental data are in the uncertainty region when  $x_{Zn} < 0.5$ , and the largest error is around  $x_{Zn} = 0.52$  with  $\ln a_{Zn} = -1.66$  from experiments<sup>18</sup> compared with -3.35 calculated from the present model. For  $\beta$ ,  $\ln a_{Zn} = -10.33$  from experiments<sup>18</sup> at  $x_{Zn} = 0.3$  are closer to the lower limit of the uncertainty region, where  $\ln a_{Zn}$  at the lower uncertainty is -10.81. The shaded ranges in Figure 8 decrease with increasing  $x_{Zn}$ , indicating a larger uncertainty of activity occurs in the Pd rich region.



Figure 9 plots the enthalpy of formation of the Pd-Zn phases at 1273 K and 300 K from the present model and available experimental data <sup>10,18,19</sup>, along with the calculated results from the previous CALPHAD modeling <sup>9</sup> at 300 K and the present first-principles results of the  $\gamma$ -phase at 0 K and high temperatures. The enthalpy of formation at 1273 K agrees reasonably well with experimental data <sup>18,19</sup>. The enthalpy of formation of  $\beta_1$  at  $x_{Zn} = 0.5$  and 1273 K is -70.1 kJ/mol-atom from the present work, compared with  $-73.9 \pm 10$  kJ/mol-atom measured by Chiang et al. <sup>18</sup> and -66.6 kJ/mol-atom measured by Kou et al. <sup>19</sup>. Figure 9 shows that the enthalpy of formation of  $\gamma$  from the present model has better agreement with experiments than the previous model <sup>9</sup>. At  $x_{Zn} = 0.8$ , the enthalpy of formation value of  $\gamma$  from the present model is -40.6 kJ/mol-atom at 300 K and from the previous model <sup>9</sup> is -48.5 kJ/mol-atom, compared with -35.1 kJ/mol-atom measured by Amore et al. <sup>10</sup>.

### 4.3 Site occupancy in the $\gamma$ -phase and surface construction

Figure 10 shows the calculated site fractions in  $\gamma$  at 773 K and 1023 K from the present model in comparison with XRD results by Edström et al. <sup>8</sup>, Gourdon et al. <sup>20</sup> and Dasgupta et al. <sup>4</sup>. Temperature has little influence on the site fraction of the  $\gamma$ -phase. With increasing Pd content, Pd is predicted to first occupy the OT sublattice, and then the OH sublattice after the OT sublattice is fully occupied. The site fractions of Pd in the OH sublattice are in good agreement with experimental data. For example, at  $x_{Pd} = 0.173$ , the calculated site fraction of Pd in the OH sublattice  $y_{Pd}^{OH}$  is 0.08, slightly higher than 0.07 measured by Dasgupta et al. <sup>4</sup>. At  $x_{Pd} = 0.181$ , 0.192, and 0.23, the calculated  $y_{Pd}^{OH}$  values are 0.118, 0.165, and 0.333, respectively, which agree well with experimental data with mean absolute error of 0.002. The Vizdal et al. <sup>9</sup> model could not predict site fractions in  $\gamma$  due to the 2-sublattice model used.

Force constants can be used to quantitatively understand interactions between atomic pairs <sup>43</sup>. A large and positive force constant suggests strong bonding interaction of an atomic pair, whereas a negative force constant indicates the tendency to separate [40]. To understand site occupancy of Pd in  $\gamma$ , we examined energies and force constants in three Pd<sub>9</sub>Zn<sub>43</sub> configurations to analyze the occupancy of an additional Pd atom compared to the full Pd OT occupation in Pd<sub>8</sub>Zn<sub>44</sub>. Three configurations are (Pd<sub>8</sub>)<sup>OT</sup>(Pd<sub>1</sub>Zn<sub>11</sub>)<sup>OH</sup>(Zn<sub>8</sub>)<sup>IT</sup>(Zn<sub>24</sub>)<sup>CO</sup>, (Pd<sub>8</sub>)<sup>OT</sup>(Zn<sub>12</sub>)<sup>OH</sup>(Pd<sub>1</sub>Zn<sub>7</sub>)<sup>IT</sup>(Zn<sub>24</sub>)<sup>CO</sup>, and (Pd<sub>8</sub>)<sup>OT</sup>(Zn<sub>12</sub>)<sup>OH</sup>(Zn<sub>8</sub>)<sup>IT</sup>(Pd<sub>1</sub>Zn<sub>23</sub>)<sup>CO</sup>, where 8 Pd atoms occupy 8 OT sites and the 9th Pd atom occupies one of the OH (conf\_OH), IT (conf\_IT), or CO (conf\_CO) sites, respectively. Force constants can be predicted by DFT-based phonon calculations <sup>44</sup>. Table 2 lists details of phonon calculations for Pd<sub>9</sub>Zn<sub>43</sub> configurations. Figure 11 shows the force constants of atomic pairs Pd-Pd, Pd-Zn, and Zn-Zn in three Pd<sub>9</sub>Zn<sub>43</sub> configurations. The Pd-Zn atomic pairs have the largest force constants 5.373 eV/Å<sup>2</sup>, compared with 4.875 eV/Å<sup>2</sup> of Pd-Pd and 3.569 eV/Å<sup>2</sup> of Zn-Zn pairs. It indicates that Pd-Zn pairs has the strongest bonding in the configuration. Table 8 shows the energy and bonding in three Pd<sub>9</sub>Zn<sub>43</sub> configurations, i.e., conf\_OH, conf\_IT, and conf\_CO. conf\_OH has the lowest energy  $E_{\text{conf\_OH}} = -105.30$  eV/atom and the shortest Pd-Zn bonding distance  $d_{\text{conf\_OH}}^{\text{Pd-Zn}} = 2.538$  Å in comparison with conf\_CO and conf\_IT. In contrast,  $d_{\text{conf\_OH}}^{\text{Pd-Pd}} = 2.940$  Å is larger than that of conf\_OH and conf\_IT. Table 8 also shows the bonding of the 9th Pd when occupying OH, CO, and IT. In conf\_OH, the 9th Pd are bonding with Zn atoms in its first nearest neighbors ( $d^{1NN} < 3.2$  Å, seen in Figure 11), with the nearest Pd atom is 4.713 Å away. In conf\_CO and conf\_IT, there are Pd-Pd pairs in the first nearest neighbors of the 9th Pd, which make the bonding between Pd and surroundings weaker than that

in conf\_OH. We conclude that the stability preference for OH occupancy of additional Pd atoms results from stronger Pd-Zn bonding interactions.

Site fractions of  $\gamma$  phase calculated from the CALPHAD modeling are further applied to analyze the surface structures. The possible stable composition of  $\gamma$  phase is evaluated ranging from Pd<sub>8</sub>Zn<sub>44</sub> to Pd<sub>12</sub>Zn<sub>40</sub> from the present model. It indicates that site occupancy in OH will be changed with changing Pd composition in  $\gamma$  phase, with OT remained being occupied by Pd, IT and CO occupied by Zn. DFT-based calculations have suggested that the (1 $\bar{1}$ 0) surface of the  $\gamma$  phase has a lower surface energy than (110) and {111} <sup>4</sup>. Figure 12 shows (1 $\bar{1}$ 0) surface constructions of  $\gamma$  phase. OT sites separately locate on the surface, forming Pd monomers (Pd<sub>1</sub>). When increase Pd occupy OH sites, OT-OH-OT assembles on the surface can then become Pd trimers (Pd<sub>3</sub>). The ability to control the exposure of specific surface ensembles between Pd<sub>1</sub> and Pd<sub>3</sub> sites is a direct consequence of the site occupancies of the bulk structure and has catalytic consequences. For example, the activity for ethylene hydrogenation and selectivity for acetylene semi-hydrogenation were drastically altered by tuning active ensembles between Pd monomers (Pd<sub>1</sub>) and Pd trimers (Pd<sub>3</sub>) <sup>4</sup>.

## 5 Conclusions

Thermodynamic modeling of the Pd-Zn system based on the CALPHAD approach has been performed with thermochemical and phase equilibria data from experiments in the literature and DFT-based total energy and phonon calculations in the present work. A 4-sublattice model is used to describe the  $\gamma$  phase in accordance with its four Wyckoff positions providing a better prediction of surface construction and enabling the understanding of active surface ensembles for catalysts.

DFT-based first-principles calculations are used to obtain Gibbs energies of endmembers for the  $\gamma$  phase. High throughput CALPHAD modeling tools (i.e., ESPEI and PyCalphad) are employed to evaluate model parameters. Uncertainty of both phase boundaries and activity are quantified in the present work. In the  $\gamma$  phase, Pd atoms first occupy the OT sublattice followed by the OH sublattice, as indicated by DFT-based total energy and phonon calculations supported by the bonding distance and force constants analyses and in agreement with experimental data. Site fractions calculated from the CALPHAD modeling contributes to analyze surface construction of  $\gamma$  phase, thus implicates to further tailor and understand active assemblies on the surface with improved catalytic performance.

### **Acknowledgments**

The authors acknowledge the financial support by the Department of Energy (DOE) via Award No. DE-SC0020147. First-principles calculations were performed partially on the Roar supercomputer at the Pennsylvania State University's Institute for Computational and Data Sciences (ICDS), partially on the resources of the National Energy Research Scientific Computing Center (NERSC) supported by the U.S. DOE Office of Science User Facility operated under Contract No. DE-AC02-05CH11231, and partially on the resources of the Extreme Science and Engineering Discovery Environment (XSEDE) supported by NSF with Grant No. ACI-1548562.

## References:

- 1 D. Teschner, E. Vass, M. Hävecker, S. Zafeiratos, P. Schnörch, H. Sauer, A. Knop-Gericke, R. Schlögl, M. Chamam, A. Wootsch, A. S. Canning, J. J. Gamman, S. D. Jackson, J. McGregor and L. F. Gladden, Alkyne hydrogenation over Pd catalysts: A new paradigm, *J. Catal.*, 2006, **242**, 26–37.
- 2 H. Zhou, X. Yang, L. Li, X. Liu, Y. Huang, X. Pan, A. Wang, J. Li and T. Zhang, PdZn Intermetallic Nanostructure with Pd-Zn-Pd Ensembles for Highly Active and Chemoselective Semi-Hydrogenation of Acetylene, *ACS Catal.*, 2016, **6**, 1054–1061.
- 3 A. Sarkany, Z. Zsoldos, B. Furlong, J. W. Hightower and L. Guzzi, Hydrogenation of 1-Butene and 1,3-Butadiene Mixtures over Pd/ZnO Catalysts, *J. Catal.*, 1993, **141**, 566–582.
- 4 A. Dasgupta, H. He, R. Gong, S.-L. Shang, E. K. Zimmerer, R. J. Meyer, Z.-K. Liu, M. J. Janik and R. M. Rioux, Atomic control of active-site ensembles in ordered alloys to enhance hydrogenation selectivity, *Nat. Chem.*, 2022, 1–7.
- 5 T. Conant, A. M. Karim, V. Lebarbier, Y. Wang, F. Girgsdies, R. Schlögl and A. Datye, Stability of bimetallic Pd-Zn catalysts for the steam reforming of methanol, *J. Catal.*, 2008, **257**, 64–70.
- 6 B. E. Green, C. S. Sass, L. T. Germinario, P. S. Wehner and B. L. Gustafson, Ester Hydrogenation over Pd-Zn/SiO<sub>2</sub>, *J. Catal.*, 1993, **140**, 406–417.
- 7 A. Dasgupta, E. K. Zimmerer, R. J. Meyer and R. M. Rioux, Generalized approach for the synthesis of silica supported Pd-Zn, Cu-Zn and Ni-Zn gamma brass phase nanoparticles, *Catal. Today*, 2019, **334**, 231–242.
- 8 V.-A. Edström, S. Westman, S. E. Rasmussen, O. Smidsrød, A. A. Lindberg, G. Jansen, B. Lamm and B. Samuelsson, *Acta Chem. Scand.*, 1969, **23**, 279–285.
- 9 J. Vizdal, A. Kroupa, J. Popovic and A. Zemanova, The experimental and theoretical study of phase equilibria in the Pd-Zn (-Sn) system, *Adv. Eng. Mater.*, 2006, **8**, 164–176.
- 10 S. Amore, S. Delsante, N. Parodi and G. Borzone, Thermochemistry of Pd-In, Pd-Sn and Pd-Zn alloy systems, *Thermochim. Acta*, 2009, **481**, 1–6.
- 11 N. Saunders and A. P. Miodownik, *CALPHAD (Calculation of Phase Diagrams): A Comprehensive Guide*, Pergamon, Oxford; New York, 1998, vol. 1.
- 12 Z.-K. Liu, First-principles calculations and CALPHAD modeling of thermodynamics, *J.*

- Phase Equilibria Diffus.*, 2009, **30**, 517–534.
- 13 H. L. LUKAS, S. G. FRIES and B. SUNDMAN, *Computational Thermodynamics: The Calphad Method*, Cambridge University Press, 2007.
  - 14 B. Bocklund, R. Otis, A. Egorov, A. Obaied, I. Roslyakova and Z. K. Liu, ESPEI for efficient thermodynamic database development, modification, and uncertainty quantification: Application to Cu-Mg, *MRS Commun.*, 2019, **9**, 618–627.
  - 15 R. Otis and Z.-K. Liu, pycalphad: CALPHAD-based Computational Thermodynamics in Python, *J. Open Res. Softw.*, 2017, **5**, 1–11.
  - 16 T. B. Massalski, *Binary Alloy Phase Diagrams*, ASM International, Ohio, 2nd edn., 1996.
  - 17 Max Hansen and Kurt Anderko, *Constitution of binary alloys*, McGraw-Hill, New York, 2nd edn., 1958.
  - 18 T. Chiang, H. Ipsier and Y. Chang, Thermodynamic properties of Pd-Zn alloys, *Zeitschrift fur Met.*, 1977, **68**, 141.
  - 19 S. Kou and Y. A. Chang, Thermodynamics of ordered  $\beta$ 1-pdZn alloys, *Acta Metall.*, , DOI:10.1016/0001-6160(75)90036-X.
  - 20 O. Gourdon and G. J. Miller, Intergrowth compounds in the Zn-rich Zn-Pd system: Toward 1D quasicrystal approximants, *Chem. Mater.*, 2006, **18**, 1848–1856.
  - 21 S. L. Shang, Y. Wang, D. E. Kim and Z. K. Liu, First-principles thermodynamics from phonon and Debye model: Application to Ni and Ni<sub>3</sub>Al, *Comput. Mater. Sci.*, 2010, **47**, 1040–1048.
  - 22 Y. Wang, Z. K. Liu and L. Q. Chen, Thermodynamic properties of Al, Ni, NiAl, and Ni<sub>3</sub>Al from first-principles calculations, *Acta Mater.*, 2004, **52**, 2665–2671.
  - 23 A. Van de Walle and G. Ceder, The effect of lattice vibrations on substitutional alloy thermodynamics, *Rev. Mod. Phys.*, 2002, **74**, 11–45.
  - 24 G. Kresse, J. Furthmuller, J. Furthmüller, J. Furthmuller, J. Furthmüller, J. Furthmueller, J. Furthmuller and J. Furthmüller, Efficient iterative schemes for ab initio total-energy calculations using a plane-wave basis set, *Phys. Rev. B-Condensed Matter*, 1996, **54**, 11169–11186.
  - 25 P. E. Blöchl, Projector augmented-wave method, *Phys. Rev. B*, 1994, **50**, 17953–17979.
  - 26 D. Joubert, From ultrasoft pseudopotentials to the projector augmented-wave method,

- Phys. Rev. B - Condens. Matter Mater. Phys.*, 1999, **59**, 1758–1775.
- 27 J. P. Perdew, K. Burke and M. Ernzerhof, Generalized gradient approximation made simple, *Phys. Rev. Lett.*, 1996, **77**, 3865–3868.
- 28 J. Heyd, G. E. Scuseria and M. Ernzerhof, Hybrid functionals based on a screened Coulomb potential, *J. Chem. Phys.*, 2003, **118**, 8207–8215.
- 29 J. Heyd, G. E. Scuseria and M. Ernzerhof, Erratum: Hybrid functionals based on a screened Coulomb potential (Journal of Chemical Physics (2003) 118 (8207)), *J. Chem. Phys.*, , DOI:10.1063/1.2204597.
- 30 Z.-K. Liu and Y. Wang, *Computational thermodynamics of materials*, Cambridge University Press, 2016.
- 31 Y. Wang, L. Q. Chen and Z. K. Liu, YPHON: A package for calculating phonons of polar materials, *Comput. Phys. Commun.*, 2014, **185**, 2950–2968.
- 32 A. T. Dinsdale, SGTE data for pure elements, *Calphad*, 1991, **15**, 317–425.
- 33 O. Redlich and A. T. Kister, Algebraic Representation of Thermodynamic Properties and the Classification of Solutions, *Ind. Eng. Chem.*, 1948, **40**, 345–348.
- 34 Z. K. Liu, Computational thermodynamics and its applications, *Acta Mater.*, 2020, **200**, 745–792.
- 35 N. H. Paulson, B. J. Bocklund, R. A. Otis, Z. K. Liu and M. Stan, Quantified uncertainty in thermodynamic modeling for materials design, *Acta Mater.*, 2019, **174**, 9–15.
- 36 H. H. Stadelmaier and W. K. Hardy, Ternäre Kohlenstofflegierungen von Palladium und Platin mit Magnesium, Aluminium, Zink, Gallium, Germanium, Kadmium, Indium, Zinn, Quecksilber, Thallium und Blei, *Zeitschrift für Met.*, 1961, **52**, 391–396.
- 37 J. P. Neumann, H. Ipsen and Y. A. Chang, The structural stability of the B2 and L10 phases in the system PdZn, *J. Less-Common Met.*, 1978, **57**, 29–37.
- 38 O. Gourdon, Z. Izaola, L. Elcoro, V. Petricek and G. J. Miller, Zn<sub>1</sub> - XP<sub>x</sub> ( x = 0.14-0.24): A missing link between intergrowth compounds and quasicrystal approximants, *Philos. Mag.*, 2006, **86**, 419–425.
- 39 S. L. Shang, B. C. Zhou, W. Y. Wang, A. J. Ross, X. L. Liu, Y. J. Hu, H. Z. Fang, Y. Wang and Z. K. Liu, A comprehensive first-principles study of pure elements: Vacancy formation and migration energies and self-diffusion coefficients, *Acta Mater.*, 2016, **109**,

- 128–141.
- 40 S. Shang, Y. Wang, R. Arroyave and Z. K. Liu, Phase stability in  $\alpha$  -  $\beta$  - rhombohedral boron, *Phys. Rev. B - Condens. Matter Mater. Phys.*, 2007, **75**, 092101.
- 41 H. Nowotny, E. Bauer and A. Stempf, Ein Beitrag zum System Palladium--Zink., *Monatsh. Chem*, 1951, **82**, 1086.
- 42 K. M. Alasafi, T. Chattopadhyay and K. Schubert, Zur Mischung PdZnN, *J. Less Common Met.*, 1978, **59**, P41–P50.
- 43 S. L. Shang, L. G. Hector, Y. Wang, H. Zhang and Z. K. Liu, First-principles study of elastic and phonon properties of the heavy fermion compound CeMg, *J. Phys. Condens. Matter*, , DOI:10.1088/0953-8984/21/24/246001.
- 44 S. L. Shang, Y. Wang, B. Gleeson and Z. K. Liu, Understanding slow-growing alumina scale mediated by reactive elements: Perspective via local metal-oxygen bonding strength, *Scr. Mater.*, 2018, **150**, 139–142.
- 45 J. W. Arblaster, Crystallographic properties of palladium, *Platin. Met. Rev.*, 2012, **56**, 181–189.
- 46 E. R. Jette and F. Foote, Precision Determination of Lattice Constants, *J. Chem. Phys.*, 1935, **3**, 605.



## Tables and Table Captions

Table 1. Crystallographic information for phases in the Pd-Zn system and their sublattice models used in the present CALPHAD modeling; where Va indicates vacancy.

Phase name	Strukturbericht	Space group	Pearson symbol	Model
Liquid(L)				(Pd,Zn)
FCC	A1	Fm $\bar{3}$ m	cF4	(Pd,Zn)
HCP	A3	P6 <sub>3</sub> /mmc	hP2	(Pd,Zn)
BCC_B2( $\beta$ )	B2	Pm $\bar{3}$ m	cP2	(Pd,Zn) <sub>1</sub> (Pd,Zn) <sub>1</sub>
FCC_L10( $\beta_1$ )	L10	P4/mmm	tP4(tP2)	(Pd,Zn) <sub>1</sub> (Pd,Zn) <sub>1</sub>
Gamma( $\gamma$ )	D8 <sub>2</sub>	I4 $\bar{3}$ m	cI52	(Pd,Zn) <sub>2</sub> (Pd,Zn) <sub>3</sub> (Pd,Zn) <sub>2</sub> (Pd,Zn) <sub>6</sub>
Pd <sub>2</sub> Zn		Pnma	oP12(C23)	(Pd) <sub>2</sub> (Zn) <sub>1</sub>
PdZn <sub>2</sub>		Cmmm	oC48(oS48)	(Pd) <sub>1</sub> (Zn) <sub>2</sub>
Pd <sub>9</sub> Zn <sub>91</sub>				(Pd) <sub>0.09</sub> (Zn) <sub>0.91</sub>

Table 2. Details of DFT-based first-principles and phonon calculations for each compound or element, including space group, total atom(s) in the cell for the calculations,  $k$ -points meshes for structure relaxations and the final static calculations (indicated by DFT), supercell sizes for phonon calculations, and  $k$ -points meshes for phonon calculations.

Compounds	Space group	Atom(s) in the cell	$k$ -points for DFT	Supercell for phonon	$k$ -points for phonon
Pd	Fm $\bar{3}$ m	1	22 $\times$ 22 $\times$ 22	3 $\times$ 3 $\times$ 3	5 $\times$ 5 $\times$ 5
Zn	P6 $_3$ /mmc	2	24 $\times$ 24 $\times$ 24	$\begin{bmatrix} -1 & 2 & 1 \\ -3 & -2 & -1 \\ 1 & -2 & 1 \end{bmatrix}$	4 $\times$ 4 $\times$ 4
Pd $_2$ Zn	Pnma	12	12 $\times$ 12 $\times$ 12	$\begin{bmatrix} -1 & 0 & -1 \\ -1 & 0 & 1 \\ 0 & 2 & 0 \end{bmatrix}$	4 $\times$ 4 $\times$ 4
PdZn	P4/mmm	2	19 $\times$ 19 $\times$ 14	3 $\times$ 3 $\times$ 3	5 $\times$ 5 $\times$ 5
PdZn $_2$	Cmm2	48	7 $\times$ 7 $\times$ 4	1 $\times$ 1 $\times$ 1	4 $\times$ 4 $\times$ 4
Pd $_8$ Zn $_{44}$	I4 $\bar{3}$ m	52	4 $\times$ 4 $\times$ 4	1 $\times$ 1 $\times$ 1	4 $\times$ 4 $\times$ 4
Endmembers of $\gamma$ -phase	N/A	26	8 $\times$ 8 $\times$ 8	N/A	N/A
Pd $_9$ Zn $_{43}$ <sup>a</sup>	I4 $\bar{3}$ m	52	3 $\times$ 3 $\times$ 3	1 $\times$ 1 $\times$ 1	2 $\times$ 2 $\times$ 2

<sup>a</sup> Three Pd $_9$ Zn $_{43}$  configurations used for analysis of site occupancy as discussed in Sec.4.3.

Table 3. Predicted lattice parameters of fcc-Pd, hcp-Zn, Pd<sub>2</sub>Zn, PdZn<sub>2</sub>, and  $\gamma$  by first-principles calculations from the relaxed structures at 0 K, together with available experimental (Expt.) data for comparison.

Phases	a (Å)	b (Å)	c (Å)	Source
fcc-Pd	3.9309			This work
	3.8902			Expt. <sup>45</sup>
hcp-Zn	2.6426		5.0268	This work
	2.6594		4.9328	Expt. <sup>46</sup>
Pd <sub>2</sub> Zn	5.3975	4.1917	7.8343	This work
	5.3500	4.1400	7.6500	Expt. <sup>36</sup>
PdZn <sub>2</sub>	7.4235	7.5773	12.3196	This work
	7.3630	7.5250	12.3070	Expt. <sup>42</sup>
$\gamma$ -phase	9.1024			This work
	9.1022			Expt. <sup>8</sup>
	9.0906			Expt. <sup>38</sup>

Table 4. Equilibrium volume  $V_0$ , bulk modulus  $B$ , and the first derivative of bulk modulus with respect to pressure  $B'$ , based on the present EOS fittings at 0 K in comparison with the previous DFT studies.

Phases	$V_0$ ( $\text{\AA}^3/\text{atom}$ )	$B$ (GPa)	$B'$	Source
Pd	15.300	167.9	5.51	This work
	15.340	163.3	5.50	DFT <sup>39</sup>
	14.716	195.5		Expt. <sup>39</sup>
Zn	15.336	57.5	5.20	This work
	15.491	58.6	5.01	DFT <sup>39</sup>
	15.185	73.2		Expt. <sup>39</sup>
Pd <sub>2</sub> Zn	14.824	146.0	5.38	This work
PdZn <sub>2</sub>	14.576	118.1	5.33	This work

Table 5. Predicted enthalpy of formation at 0 K,  $\Delta_f H$  (kJ/mol-atom), of  $\gamma$  and  $\beta_1$  using DFT-based calculations with GGA and HSE06 as exchange-correlation functionals, respectively, in comparison with available experimental data.

Phases	Configurations	$x_{Zn}$	$\Delta_f H$	Source
$\gamma$ -phase	Pd <sub>10</sub> Zn <sub>42</sub>	0.81	-27.9	DFT/GGA, this work
	Pd <sub>10</sub> Zn <sub>42</sub>	0.81	-33.7	DFT/HSE06, this work
	N/A	0.80	-35.1	Calorimetry, at 300 K <sup>10</sup>
$\beta_1$ -phase	PdZn	0.50	-53.7	DFT/GGA, this work
	PdZn	0.50	-69.2	DFT/HSE06, this work
	N/A	0.50	-73.9 $\pm$ 10	Vapor pressure at 1273 K <sup>18</sup>
	N/A	0.50	-66.6	Vapor pressure at 1273 K <sup>19</sup>

Table 6. Model parameters in the present CALPHAD modeling of the Pd-Zn system with Gibbs energy in J/mol-atom and temperature (T) in Kelvin.

Phase	Parameters	Value	Ref.
Liquid	$0_{\text{L}}^{\text{Liquid}}$	$-134358 - 7.478 T$	
	$1_{\text{L}}^{\text{Liquid}}$	69096	
	$2_{\text{L}}^{\text{Liquid}}$	$1643 - 5.417 T$	
FCC_A1	$0_{\text{L}}^{\text{Fcc}}$	$-207719 + 43.952 T$	
	$1_{\text{L}}^{\text{Fcc}}$	$4410 + 1 T$	
	$2_{\text{L}}^{\text{Fcc}}$	$48734 - 6.984 T$	
HCP	$0_{\text{L}}^{\text{Hcp\_zn}}$	$-134856 - 12.982 T$	
	$1_{\text{L}}^{\text{Hcp\_zn}}$	51421	
BCC_B2( $\beta$ )	$G_{\text{Pd:Pd}}^{\text{B2}}$	$2\text{GHSER}_{\text{Pd}} + 5000$	9
	$G_{\text{Pd:Zn}}^{\text{B2}}$	$\text{GHSER}_{\text{Pd}} + \text{GHSER}_{\text{Zn}} - 120961 + 16.563 T$	
	$G_{\text{Zn:Pd}}^{\text{B2}}$	$\text{GHSER}_{\text{Pd}} + \text{GHSER}_{\text{Zn}} - 120961 + 16.563 T$	
	$G_{\text{Zn:Zn}}^{\text{B2}}$	$2\text{GHSER}_{\text{Zn}} + 5000$	9
	$0_{\text{L}}^{\text{B2}}_{\text{Pd:Pd,Zn}} = 0_{\text{L}}^{\text{B2}}_{\text{Pd,Zn:Pd}}$	$-49594 + 13.968 T$	
	$1_{\text{L}}^{\text{B2}}_{\text{Pd:Pd,Zn}} = 1_{\text{L}}^{\text{B2}}_{\text{Pd,Zn:Pd}}$	22460	
	$0_{\text{L}}^{\text{B2}}_{\text{Zn:Pd,Zn}} = 0_{\text{L}}^{\text{B2}}_{\text{Pd,Zn:Zn}}$	$-94437 + 7.857 T$	
FCC_L10( $\beta_1$ )	$G_{\text{Pd:Pd}}^{\text{L10}}$	$2\text{GHSER}_{\text{Pd}} + 15000$	
	$G_{\text{Pd:Zn}}^{\text{L10}}$	$\text{GHSER}_{\text{Pd}} + \text{GHSER}_{\text{Zn}} - 134320 + 25.870 T$	9
	$G_{\text{Zn:Pd}}^{\text{L10}}$	$\text{GHSER}_{\text{Pd}} + \text{GHSER}_{\text{Zn}} - 134320 + 25.870 T$	9

---

	$G_{\text{Zn:Zn}}^{\text{L10}}$	$2\text{GHSER}_{\text{Zn}} + 15000$
	${}^0\text{L}_{\text{Pd:Pd,Zn}}^{\text{L10}} = {}^0\text{L}_{\text{Pd,Zn:Pd}}^{\text{L10}}$	$-35819 + 0.492 T$
	${}^1\text{L}_{\text{Pd:Pd,Zn}}^{\text{L10}} = {}^1\text{L}_{\text{Pd,Zn:Pd}}^{\text{L10}}$	$28503 + 1.138 T$
	${}^0\text{L}_{\text{Zn:Pd,Zn}}^{\text{L10}} = {}^0\text{L}_{\text{Pd,Zn:Zn}}^{\text{L10}}$	$-76386 + 3.498 T$
Gamma( $\gamma$ )	$G_{\text{Pd:Pd:Pd:Pd}}^{\text{Gamma}}$	$13\text{GHSER}_{\text{Pd}} + 26802$
	$G_{\text{Pd:Pd:Pd:Zn}}^{\text{Gamma}}$	$7\text{GHSER}_{\text{Pd}} + 6\text{GHSER}_{\text{Zn}} - 83241$
	$G_{\text{Pd:Pd:Zn:Pd}}^{\text{Gamma}}$	$11\text{GHSER}_{\text{Pd}} + 2\text{GHSER}_{\text{Zn}} + 131161$
	$G_{\text{Pd:Pd:Zn:Zn}}^{\text{Gamma}}$	$5\text{GHSER}_{\text{Pd}} + 8\text{GHSER}_{\text{Zn}} - 61982$
	$G_{\text{Pd:Zn:Pd:Pd}}^{\text{Gamma}}$	$10\text{GHSER}_{\text{Pd}} + 3\text{GHSER}_{\text{Zn}} + 186950$
	$G_{\text{Pd:Zn:Pd:Zn}}^{\text{Gamma}}$	$4\text{GHSER}_{\text{Pd}} + 9\text{GHSER}_{\text{Zn}} + 25785$
	$G_{\text{Pd:Zn:Zn:Pd}}^{\text{Gamma}}$	$8\text{GHSER}_{\text{Pd}} + 5\text{GHSER}_{\text{Zn}} + 259218$
	$G_{\text{Pd:Zn:Zn:Zn}}^{\text{Gamma}}$	$2\text{GHSER}_{\text{Pd}} + 11\text{GHSER}_{\text{Zn}} + 190798$
	$G_{\text{Zn:Pd:Pd:Pd}}^{\text{Gamma}}$	$11\text{GHSER}_{\text{Pd}} + 2\text{GHSER}_{\text{Zn}} - 181667$
	$G_{\text{Zn:Pd:Pd:Zn}}^{\text{Gamma}}$	$5\text{GHSER}_{\text{Pd}} + 8\text{GHSER}_{\text{Zn}} - 564558$ $+ 148.359 T$
	$G_{\text{Zn:Pd:Zn:Pd}}^{\text{Gamma}}$	$9\text{GHSER}_{\text{Pd}} + 4\text{GHSER}_{\text{Zn}} - 64329$
	$G_{\text{Zn:Pd:Zn:Zn}}^{\text{Gamma}}$	$3\text{GHSER}_{\text{Pd}} + 10\text{GHSER}_{\text{Zn}} - 411154$
	$G_{\text{Zn:Zn:Pd:Pd}}^{\text{Gamma}}$	$8\text{GHSER}_{\text{Pd}} + 5\text{GHSER}_{\text{Zn}} - 13907$
	$G_{\text{Zn:Zn:Pd:Zn}}^{\text{Gamma}}$	$2\text{GHSER}_{\text{Pd}} + 11\text{GHSER}_{\text{Zn}} - 440291$ $+ 23.439 T$
	$G_{\text{Zn:Zn:Zn:Pd}}^{\text{Gamma}}$	$6\text{GHSER}_{\text{Pd}} + 7\text{GHSER}_{\text{Zn}} + 26798$

---

---

	$G_{\text{Zn:Zn:Zn:Zn}}^{\text{Gamma}}$	$13\text{GHSER}_{\text{Zn}} + 88131$
	${}^0L_{\text{Zn:Pd,Zn:Pd:Zn}}^{\text{Gamma}}$	$-393082$
	${}^1L_{\text{Zn:Pd,Zn:Pd:Zn}}^{\text{Gamma}}$	$-5712$
$\text{Pd}_2\text{Zn}$	$G_{\text{Pd:Zn}}^{\text{Pd}_2\text{Zn}}$	$2\text{GHSER}_{\text{Pd}} + \text{GHSER}_{\text{Zn}} - 142996 + 18.662 T$
$\text{PdZn}_2$	$G_{\text{Pd:Zn}}^{\text{PdZn}_2}$	$\text{GHSER}_{\text{Pd}} + 2\text{GHSER}_{\text{Zn}} - 160623 + 23.213 T$
$\text{Pd}_9\text{Zn}_{91}$	$G_{\text{Pd:Zn}}^{\text{Pd}_{0.09}\text{Zn}_{0.91}}$	$0.09\text{GHSER}_{\text{Pd}} + 0.91\text{GHSER}_{\text{Zn}} - 19059$ $- 0.290 T$

---



Table 7. Temperatures and compositions of invariant reactions in the Pd-Zn system calculated from the present CALPHAD modeling with available experimental data included.

Reaction	$x_{Zn}$			Temperature (K)	Ref.
Liquid $\rightarrow$ $\beta$ + $\gamma$	75.0	64.2	78.2	1123.3	This work
	75	65	77	1118	16
$\beta \rightarrow \beta_1$ + $\gamma$	63.2	57.3	77.5	837.6	This work
	57	55	76	838	16
$\beta_1$ + $\gamma \rightarrow$ PdZn <sub>2</sub>	57.2	77.5	66.7	799.6	This work
	56	76	66.7	803 $\pm$ 10	16
Liquid + $\gamma \rightarrow$ Pd <sub>9</sub> Zn <sub>91</sub>	97.7	84.6	91.0	707.2	This work
	98	85	92	703	17
				707	9
Liquid $\rightarrow$ Pd <sub>9</sub> Zn <sub>91</sub> + HCP	98.2	91.0	99.0	681.1	This work
				690	9

Table 8. Energies, and distances of bonds (d) for three Pd<sub>9</sub>Zn<sub>43</sub> configurations with the first 8 Pd atoms occupying the OT site, and the 9<sup>th</sup> Pd atom (Pd<sup>9th</sup>) occupying the OH, CO, or IT site, denoted by conf\_OH, conf\_CO, and conf\_IT, respectively. Configurations are relaxed using DFT calculations.

Configuration	Energy (eV/atom)	d of Pd-Zn <sup>a</sup> (Å)	d of Pd-Pd <sup>b</sup> (Å)	d of Pd <sup>9th</sup> -Zn <sup>c</sup> (Å)	d of Pd <sup>9th</sup> -Pd <sup>d</sup> (Å)
conf_OH	-105.30	2.538	2.940	2.563	4.713
conf_CO	-104.89	2.558	2.783	2.562	2.783
conf_IT	-104.74	2.560	2.887	2.613	3.192

<sup>a</sup> Distance of the nearest Pd-Zn pair in the configuration (Å).

<sup>b</sup> Distance of the nearest Pd-Pd pair in the configuration (Å).

<sup>c</sup> Distance of the nearest Pd-Zn pair around the 9<sup>th</sup> Pd atom (Å).

<sup>d</sup> Distance of the nearest Pd-Pd pair around the 9<sup>th</sup> Pd atom (Å).

## Figures and Figure Captions

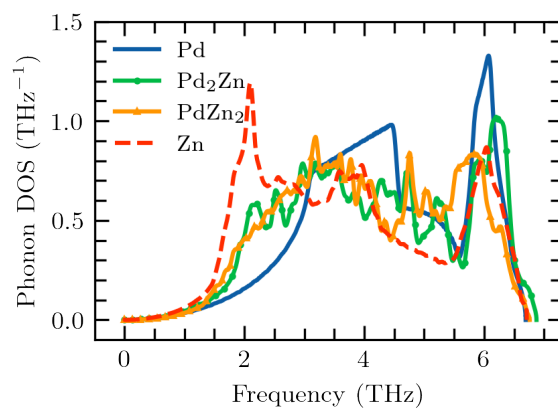


Figure 1. Predicted phonon DOS's of Pd, Zn, Pd<sub>2</sub>Zn, and PdZn<sub>2</sub> from the DFT-based phonon calculations.

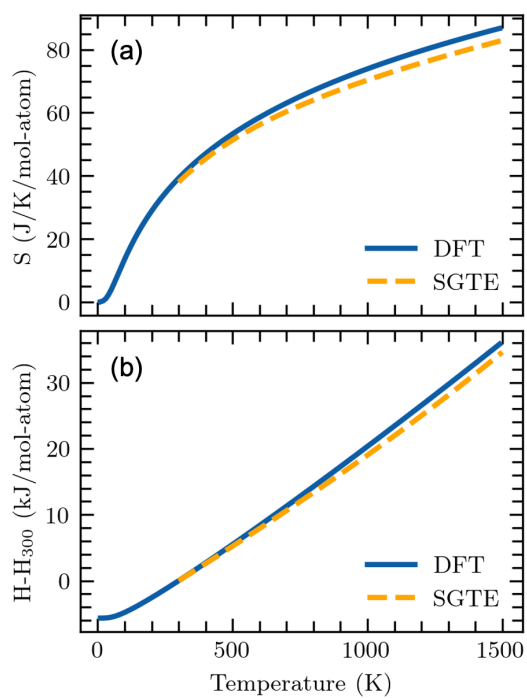


Figure 2. Comparison of the (a) entropy and (b) enthalpy of Pd from the DFT-based phonon calculations to the SGTE data<sup>32</sup>.

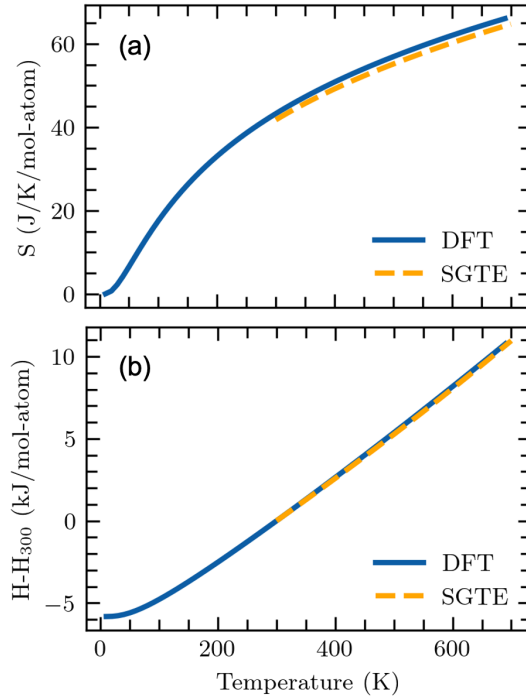


Figure 3. Comparison of the entropy and enthalpy of Zn from the phonon calculations to the SGTE data<sup>32</sup>.

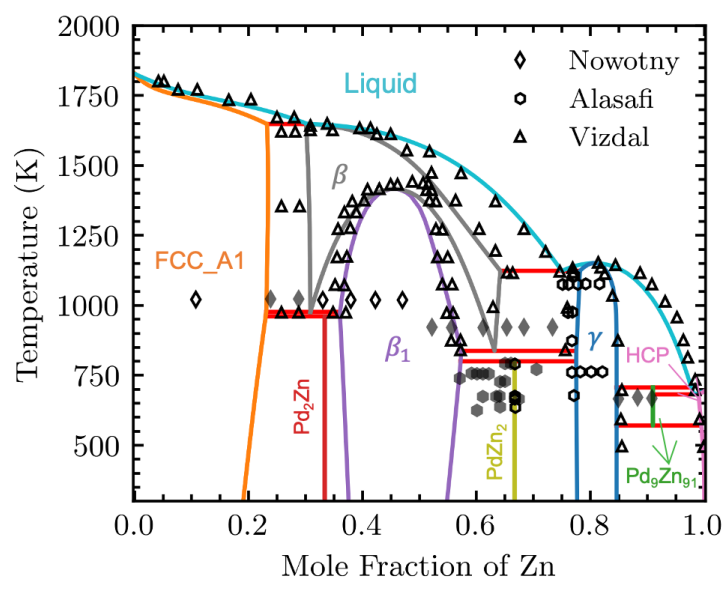


Figure 4. Calculated phase diagram from the present CALPHAD modeling in comparison with experimental data from Nowotny et al.<sup>41</sup> (diamonds), Alasafi et al.<sup>42</sup> (hexagons), and experimental data summarized by Vizdal et al.<sup>9</sup> (triangles). Hollow diamonds and hexagons represent single

phase region and shadowed diamonds and hexagons represent two phases region reported by Nowotny et al.<sup>41</sup> and Alasafi et al.<sup>42</sup>.

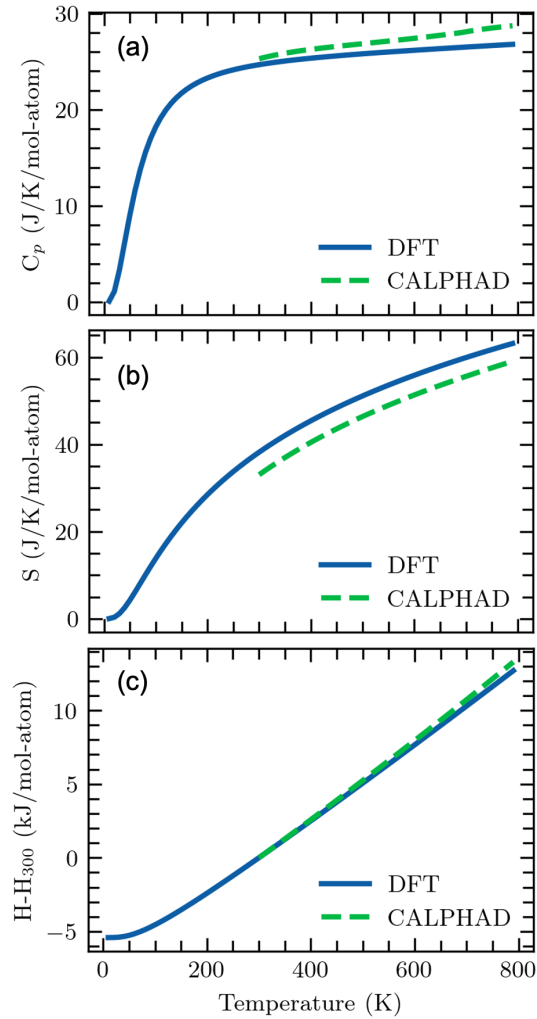
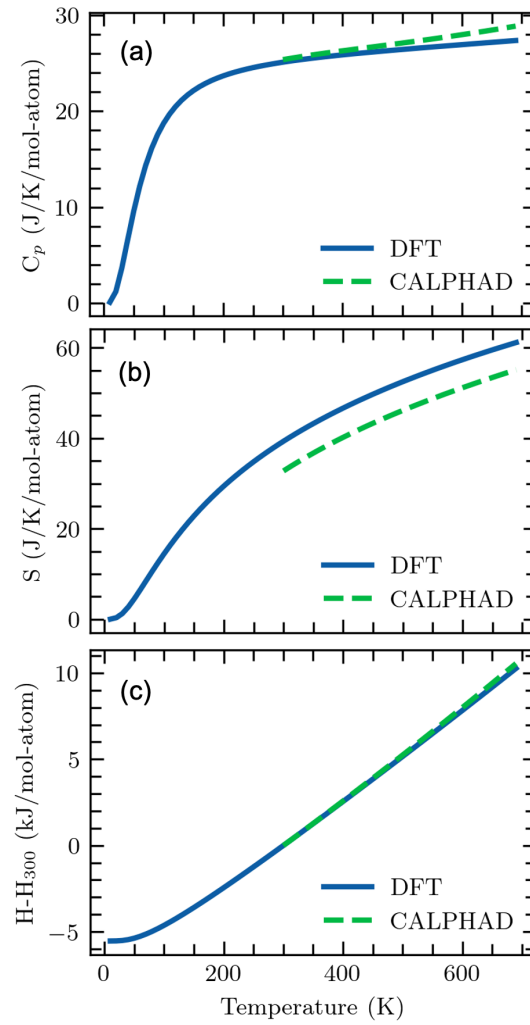


Figure 5. Predicted (a) heat capacity, (b) entropy, and (c) enthalpy of Pd<sub>2</sub>Zn using the DFT-based phonon calculations, compared with those from the present CALPHAD modeling.



*Figure 6.* Heat (a) capacity, (b) entropy, and (c) enthalpy of PdZn<sub>2</sub> using the phonon calculations from first-principles calculations, compared with those from the present CALPHAD modeling.

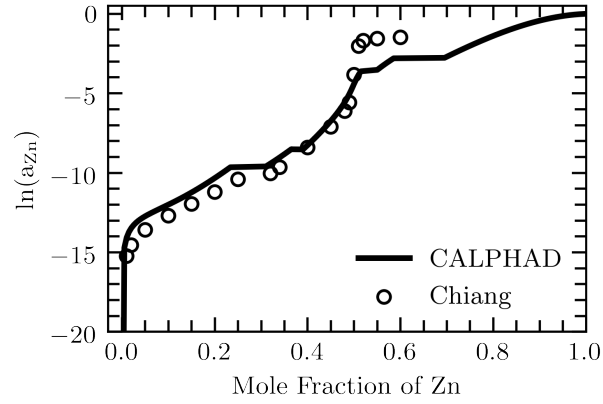


Figure 7. Calculated activity of Zn at 1273 K with experimental data measured by Chiang et al.<sup>18</sup> superimposed.

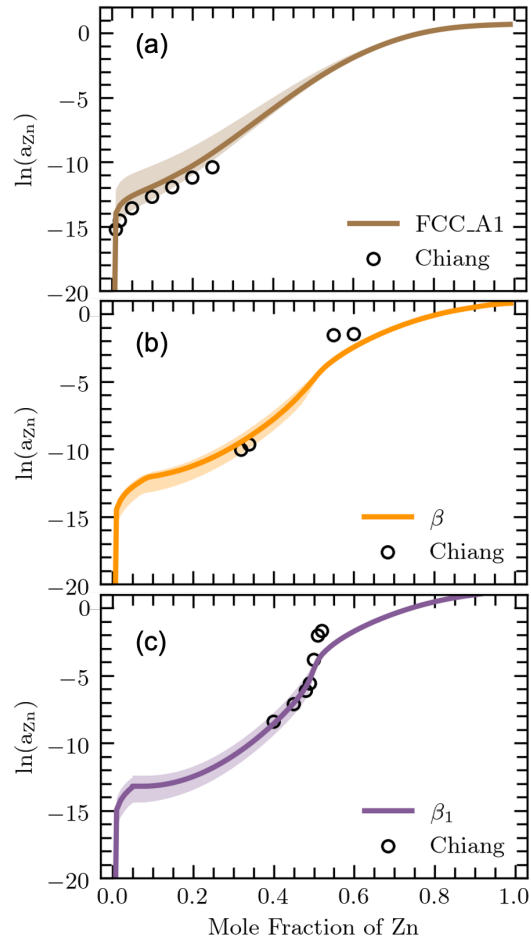


Figure 8. Uncertainty quantification of activity of (a) FCC, (c)  $\beta$ , and (d)  $\beta_1$ , marked in the shaded regions with corresponding color of each phase.

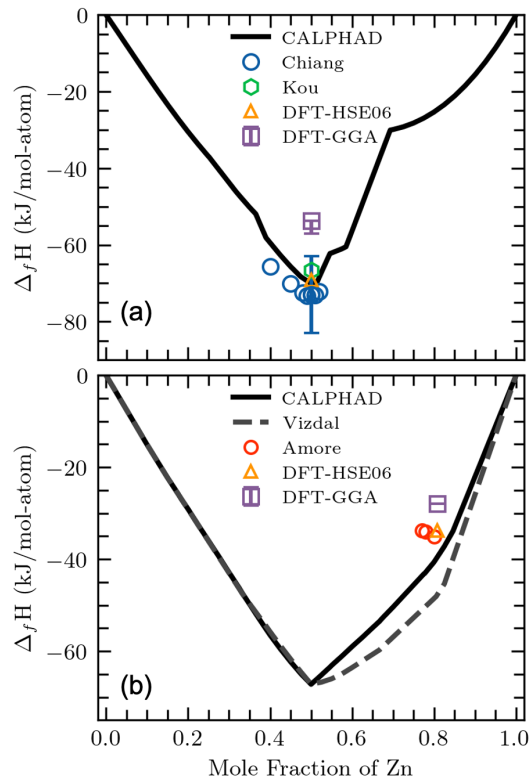


Figure 9. Calculated enthalpy of formation at (a) 1273 K and (b) 300 K, along with DFT-based calculations and available experimental data by Chiang et al.<sup>18</sup>, Kou and Chang<sup>19</sup>, and Amore et al.<sup>10</sup>. DFT using HSE are calculated at 0 K. DFT using GGA are calculated at 0 K and high temperatures 300 K and 1270 K respectively, showing as purple bars in the figure.



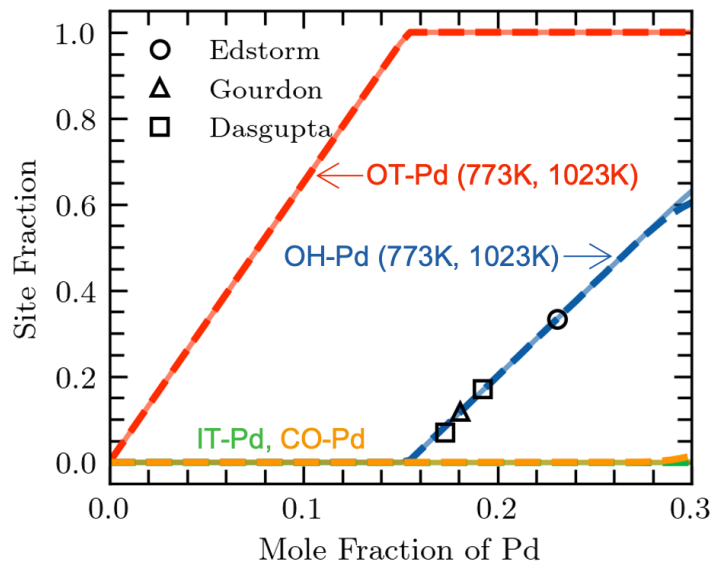


Figure 10. Calculated site fractions in  $\gamma$  at 773K (solid lines) and 1023 K (dash lines) with the experimental data by Edström et al. at 923 K<sup>8</sup>, Gourdon et al. at 1023 K<sup>20</sup>, and Dasgupta et al. at 773 K<sup>4</sup> superimposed.

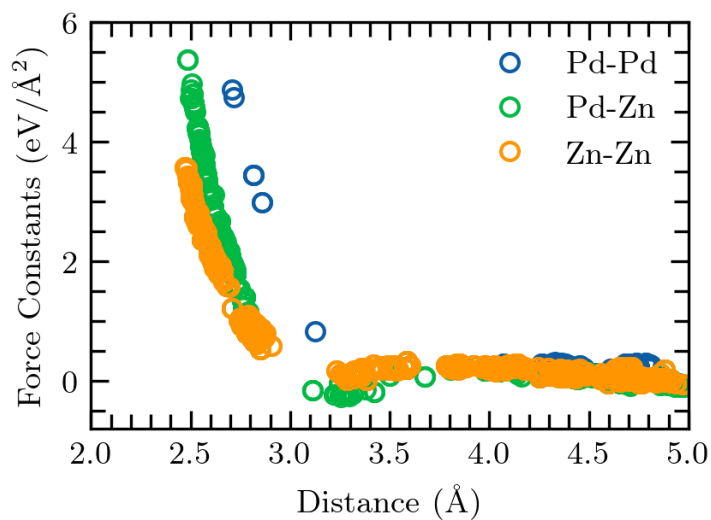
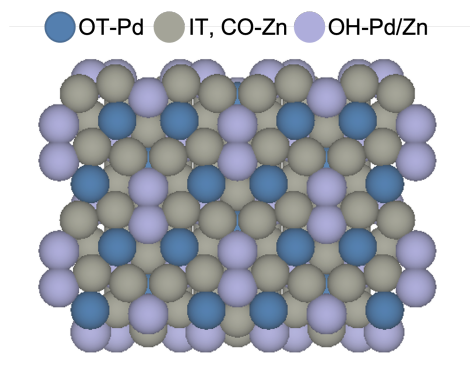


Figure 11. Force constants of Pd-Pd, Pd-Zn, and Zn-Zn atom pairs in Pd<sub>9</sub>Zn<sub>43</sub> configurations obtained from phonon calculations.



*Figure 12.*  $(1\bar{1}0)$  surface of  $\gamma$  in  $2 \times 2 \times 2$  supercell. Blue atoms are OT sites, which are occupied by Pd atoms. Grey atoms are IT and CO sites, which are occupied by Zn atoms. Purple atoms are OH sites, which can be occupied by both Pd and Zn atoms.